



City Research Online

City, University of London Institutional Repository

Citation: Lu, Y., Rane, S. & Kovacevic, A. (2022). Evaluation of cut cell cartesian method for simulation of a hook and claw type hydrogen pump. *International Journal of Hydrogen Energy*, 47(54), pp. 23006-23018. doi: 10.1016/j.ijhydene.2022.05.110

This is the published version of the paper.

This version of the publication may differ from the final published version.

Permanent repository link: <https://openaccess.city.ac.uk/id/eprint/28383/>

Link to published version: <https://doi.org/10.1016/j.ijhydene.2022.05.110>

Copyright: City Research Online aims to make research outputs of City, University of London available to a wider audience. Copyright and Moral Rights remain with the author(s) and/or copyright holders. URLs from City Research Online may be freely distributed and linked to.

Reuse: Copies of full items can be used for personal research or study, educational, or not-for-profit purposes without prior permission or charge. Provided that the authors, title and full bibliographic details are credited, a hyperlink and/or URL is given for the original metadata page and the content is not changed in any way.

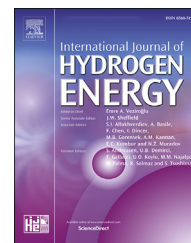
City Research Online:

<http://openaccess.city.ac.uk/>

publications@city.ac.uk

Available online at www.sciencedirect.com

ScienceDirect

journal homepage: www.elsevier.com/locate/ijhydene

Evaluation of cut cell cartesian method for simulation of a hook and claw type hydrogen pump

Yang Lu^{*}, Sham Rane, Ahmed Kouacevic

Centre for Compressor Technology, City, University of London, EC1V 0HB, London, UK

HIGHLIGHTS

- The conservation accuracy of the cut cell cartesian mesh is verified.
- A cut cell cartesian mesh is used for the simulation of a hydrogen pump.
- The simulation results are verified with experimental data.
- The volume flow rate and power of air case is comparable with the hydrogen case.

ARTICLE INFO

Article history:

Received 27 December 2021

Received in revised form

5 April 2022

Accepted 12 May 2022

Available online 3 June 2022

Keywords:

Claw pump

Cut cell cartesian method

CFD

Hydrogen recirculation

ABSTRACT

Hook and claw pumps are used for recirculation of excess hydrogen in fuel cells. Optimization of the pump design is essential. Computational Fluid Dynamic (CFD) is an effective method for performance optimization. However, it is difficult to conduct CFD simulation because of the sharp cusp of the rotor profile. Cut cell Cartesian mesh could be the solution to handle this complex and moving geometries. The aim of this paper is to evaluate ANSYS Forte for hook and claw pumps. Firstly, the conservation accuracy of the cut cell cartesian mesh is verified using an adiabatic piston cylinder case. Then, simulation results of hook and claw type pump are compared with experimental data. Finally, simulation results of air and hydrogen are compared. The results show that the CFD simulation of hook and claw pumps using cut cell cartesian mesh could provide an efficient and effective approach for the optimization of the system.

© 2022 The Author(s). Published by Elsevier Ltd on behalf of Hydrogen Energy Publications LLC. This is an open access article under the CC BY-NC-ND license (<http://creativecommons.org/licenses/by-nc-nd/4.0/>).

Introduction

Renewable energy sources such as solar, wind, and tidal power, are on the rise and becoming highly important in new energy strategies. Hydrogen is one of the prominent candidates for a cost-efficient, clean and sustainable energy carrier for future energy systems and global economic security [1]. Governments worldwide have taken historic steps towards net-zero, such as in the UK where the sale of new petrol and

diesel cars will end by 2030. One of the most promising ways to make this goal a reality is the usage of cleanly produced electricity from non-fossil fuels such as hydrogen using fuel cells technology [2]. In a fuel cell, a combination of hydrogen (coming from a storage tank) and oxygen (from the air) produces electricity, heat, and water as a by-product. Hydrogen is injected in a higher quantity to react with the oxygen. The excess hydrogen needs to be cycled back to the system by using a hydrogen recirculation pump. The working principle

^{*} Corresponding author.

E-mail address: yang.lu.4@city.ac.uk (Y. Lu).

<https://doi.org/10.1016/j.ijhydene.2022.05.110>

0360-3199/© 2022 The Author(s). Published by Elsevier Ltd on behalf of Hydrogen Energy Publications LLC. This is an open access article under the CC BY-NC-ND license (<http://creativecommons.org/licenses/by-nc-nd/4.0/>).

of the proton exchange membrane fuel cell (PEMFC) is demonstrated in Fig. 1.

Positive displacement machines such as diaphragm compressors [4], scroll compressors [3], roots blower [5,6], twin screw compressors [7] and claw pumps [8] can all be used to recirculate the hydrogen but with associated advantages and disadvantages which are explained specifically by Gu [9]. Due to the reliability, simplicity, compact, internal compression and oil-free character [10,11], the hook and claw pumps are preferable among all these positive displacement machines as hydrogen recirculation pumps in the fuel cell vehicles (FCVs).

There has been a large body of research that has sought to improve the performance of this kind of machines. The first step of the process is the design of the rotor profile. Many rotor profiles of hook and claw pumps have been proposed [11–13], allowing the geometric characteristics to be compared. Moreover, it has been shown that chamber models which were developed for the positive displacement machines can also be utilized in this form of claw pump. The chamber model was described in greater detail by Stosic [14,15]. Peng [16] used the model to predict the performance of the tooth compressors and validated the mathematical model by comparing it with experimental results. Furthermore, with the continuous increase in computer performance, the computational fluid dynamics (CFD) method has become a practical option for simulating the working process of positive displacement machines (PDMs).

The rotating rotors and the variation of the gaps are the primary challenge in generating a high-quality mesh for the simulation to achieve reliable results. In addition, rapid change in curvature of some specific rotor profiles may cause problems for mesh generation. The structured body-fitted methods are used for the simulation of the compressors and pumps. Casari [17] compared the state-of-the-art mesh generating methods: along with immersed boundaries, overset, dynamics remeshing and key frame remeshing and conclude that the custom predefined mesh generation strategy is the most suitable choice for the simulation of PDMs. SCORG is a mesh generation software for positive displacement machines, and has been successfully used to predict performance of roots blowers [18,19], air compressors [20,21], oil-injected compressors [22] and water injected compressors [23]. Gu [9] used TwinMesh to generate the body-fitted

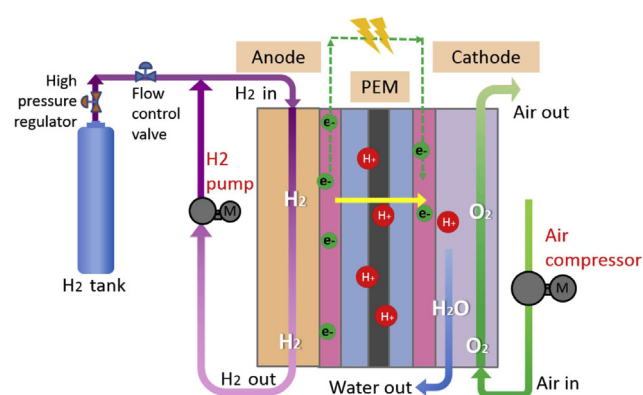


Fig. 1 – The principle of the PEMFC [3].

structure mesh for the simulation of the hook and claw pump. Dong [24] utilized an unstructured mesh for his CFD simulation and the numerical results matched well with the experimental results. The cases have been studied using body-fitted method which need a very high-resolution mesh to capture the velocity distribution. All the studies reviewed so far, however, suffer from the facts that lots of effort need to be spared on improving the mesh quality. Recently, the cut cell-based method for CFD modelling has been developed for the simulation of twin-screw compressors. The advantages of this method included how its' application to complex moving geometry required a simplified process to start the simulation due to the automation of grid generation. Commercial software like Convergent Science, Star CCM+ and ANSYS Forte have adopted this technology in commercial CFD code. The mesh generation of hook and claw profile is a challenge for transient simulation because of the presence of sharp edges and convex geometries [25], and ANSYS Forte provides cut-cell cartesian method can solve this problem. In the moving deforming mesh applications, several references [26–28] have indicated that coupled solver provides more accurate solution. This solver also found to be faster and more robust for large deformation. Rowinski [29,30] has also modelled twin screw compressors and expanders, and validated it against the experimental measurements. However, the author makes no attempt to specify the velocity vortices and temperature in the chamber of twin-screw compressors and expanders. In addition, the cut cell methods have yet to be assessed in terms of conservation and accuracy and have not previously been used for the simulation of hydrogen claw pumps.

There are two aims in this research. The first is to evaluate the conservation accuracy of the cut cell Cartesian mesh. The second is to verify the capability of the cut cell cartesian mesh with adaptive mesh refinement and gap flow model for the simulation of claw type hydrogen pump. To achieve the above aims, the adiabatic piston cylinder case is utilized to verify the volume conservation and pressure and temperature accuracy in [Evaluation of the cut cell method](#). In [The simulation of hook and claw pumps](#), the hook and claw pump is simulated under different working condition and the results verified with experimental data. In addition, operation with air and hydrogen are compared for velocity, temperature and pressure variation. The cut cell cartesian mesh with adaptive mesh refinement and gap flow model is shown to be capable of accurately simulating the claw type pump. The case is easy to setup with less user effort and the simulation process is more stable and robust comparing to body-fitted method.

Evaluation of the cut cell method

Ansys Forte uses Arbitrary-Lagrangian Eulerian (ALE) method for solving flow equations. Automatic mesh generation (AMG) and adaptive mesh refinement (AMR) are used for the mesh generation [31]. Physical domain cut by the boundary is represented by a multi-level octree mesh [32]. Mesh inside the physical domain is denoted as computational domain while mesh outside physical domain is discarded as shown in Fig. 2. The mesh is organized in an octree data structure. Boundary tracking and boundary representation methods are

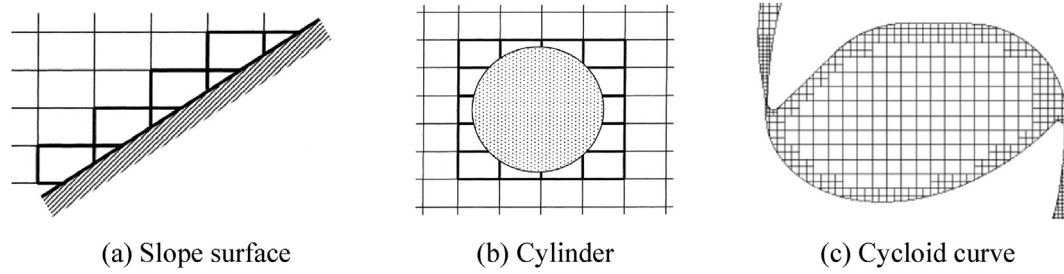


Fig. 2 – Cut-cell at solid boundary [34].

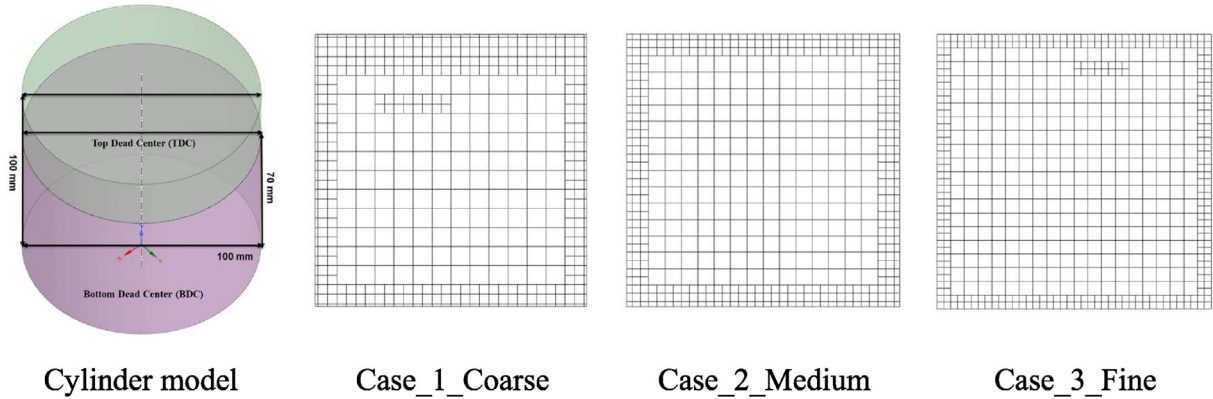


Fig. 3 – The cylinder model and cross-section mesh with different sizes.

Table 1 – Fluid properties.

	Unit	N2	O2	Air	H2
Molar mass	g/mol	28	32	29	2
Density	kg/m ³	1.142	1.301	1.176	0.082
Dynamic viscosity	10 ⁻⁵ nbsp; Pa s	1.76	2.04	1.849	0.88
Thermal conductivity	W/(kg °C)	0.0262	0.02676	0.02551	0.1820
Specific heat capacity	J/(kg °C)	1041	920	1007	14314

considered for solving moving boundary problems [33]. The reader can refer to paper [26,32] for details.

The conservation of mass, momentum, energy and other properties applied to fluid flow in a control volume (CV) can be defined by coupled, time dependent, partial differential equations which can be referenced to paper [35]. ANSYS Forte solver's gap model has been used the under-resolution of the local gap size. Cell size and wall shear resistance effect are considered in this model based on an analytical solution of shear stress in Poiseuille flow [36]. The gap shear resistance factor is based on Eq. (1). The gap model will be activated to calculate the leakage flow if the clearances are smaller than the surface proximity.

$$\frac{U_{decelerated}}{U_{original}} = f\left(\frac{1}{h^2}, v, \Delta t\right) \quad 1$$

The purpose of this analysis was to evaluate the accuracy of the cut cell cartesian mesh by comparing the results from ANSYS Forte with the theoretical results.

Table 2 – Timestep independence study.

	Timestep_1	Timestep_2	Timestep_3
Time steps per degree	0.9	1.1	11
Error in max pressure [%]	3.37	2.83	0.35
Error in max temperature [%]	3.39	2.83	0.33

Table 3 – Mesh independence analysis.

	Coarse	Medium	Fine
Element number	10.3k	15.8k	23k
Global Mesh Size	0.7	0.6	0.5
Error in max pressure [%]	-0.07	-0.04	0.03
Error in max temperature [%]	-0.04	-0.01	0.06

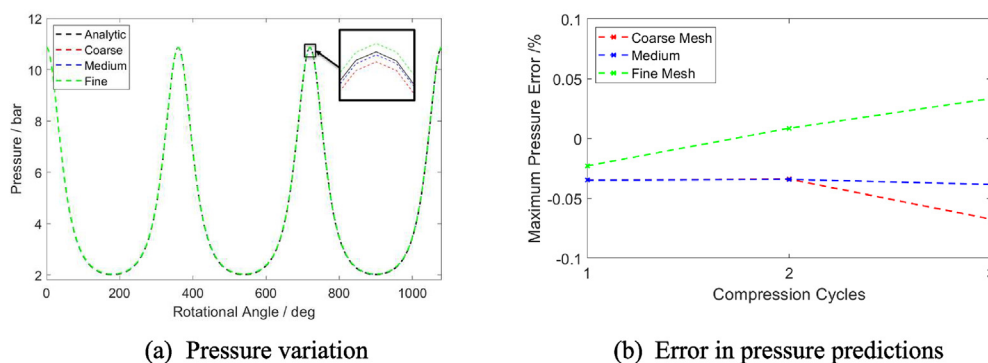


Fig. 4 – Pressure variation and error. (a) Pressure variation.

Numerical accuracy of the cut cell method

An adiabatic compression and expansion process in a piston cylinder is a simple geometry that provides a convenient case to test the mass conservation and numerical accuracy of the cut cell method for application to positive displacement machines. Rane et al. [35] have used the piston cylinder case and compared three grid deformation strategies which are the diffusion equation mesh smoothing, user defined nodal displacement and key-frame remeshing using the ANSYS CFX solver. It was seen that the key-frame remeshing has less accuracy in conservation of calculated variables. The same case and boundary conditions were used for the comparison.

A cylinder with diameter 100 mm and length 100 mm was considered as shown in Fig. 3. The rod length b , piston compression height s , crank radius r and crank angle θ follow the relation:

$$s^2 + r^2 - 2rs \cos(\theta) = b^2$$

The Piston displacement was 70 mm varying sinusoidal with a frequency of 50 Hz. The piston at the top dead center (TDC) position gives the minimum volume of $2.356 \times 10^{-4} \text{ m}^3$. The maximum cylinder volume is $7.854 \times 10^{-4} \text{ m}^3$ at bottom dead center (BDC). This gave a fixed volume ratio of 3.333 for the system. There are no leakages or flow boundaries present in the system.

The reversible adiabatic compression and expansion process in a piston cylinder without clearance was solved in this study by ANSYS Forte 2020R2. The simulation result of pressure and temperature are compared with the analytical results which are calculated by the polytropic process Eq. (2) while the polytropic index is taken 1.4 for isentropic process.

$$\frac{p_2}{p_1} = \left(\frac{v_1}{v_2} \right)^\gamma = \left(\frac{T_2}{T_1} \right)^{\frac{\gamma}{\gamma-1}} \quad 2$$

The initial position of the piston was at TDC (tope dead center) position i.e., minimum chamber volume. Therefore, the initial conditions were 10.86 bar for absolute pressure and 482.35 K for temperature. The crank speed was set at 3000 rpm. Walls are considered adiabatic. The lowest pressure and temperature are 2.013 bar and 298 K individually. The chemistry used in this case contains air (0.79% of N₂ and 0.21%

Table 4 – Rotor geometry.

Rotor Configuration	Value	Rotor Configuration	Value
Rotor combination	1by1	Inlet pipe length [mm]	20
Axis distance [mm]	45	Outlet pipe length [mm]	100
Rotor length [mm]	25	Axial clearance [mm]	0.08
Outer circle diameter [mm]	65.42	Radial gap [mm]	0.07
Inner circle diameter [mm]	24.42	Interlobe gap [mm]	0.08

Table 5 – Operating conditions and solver setup parameters.

Parameters	Value	Parameters	Value
Speed [rpm]	6000	Turbulence Model	k-epsilon
Suction Temperature [K]	300	Suction Pressure [bar]	1.01
Discharge Temperature [K]	300	Discharge Pressure [bar]	1.01–1.31
Global mesh size	0.1	Time steps size	2.5E-06

of O₂) and satisfies with the ideal gas equation $pv = nRT$. The fluid properties of nitrogen, oxygen, and hydrogen at 300 K are shown in Table 1.

Timestep independence study

ANSYS Forte uses adaptive time step control to adjust the solver's time step size for each transient flow integration step. Setting the proper timestep can not only reduce the simulation time but can also better capture the velocity and pressure variation. For rotary machines, the recommended method for deciding the Maximum simulation time step is to have at least 10-time steps per degree of rotation [37]. Using this guideline, the max time step can be calculated as Time step = $60 / (\text{RPM} \times 360 \times 10)$ which gives 5.55E-6 for 3000 rpm. To test the time step setup in ANSYS Forte, three different time steps are compared as shown in Table 2. The simulation run for 5 cycles corresponding to 1800 rotational angles. The time step has an impact on the pressure and temperature results as the errors decreased from 3.37% to 0.35% which were calculated by Eq. (3). With increasing time step, the pressure and temperature error decreased. At 11-time steps per degree, the error is below

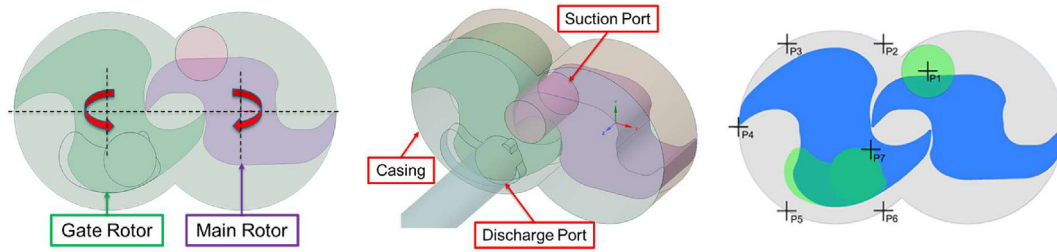


Fig. 5 – The twin screw vacuum pump rotor and location of monitor points.

Table 6 – Mesh independence analysis.

Parameters	Units	Coarse	Medium	Fine
Global mesh size	[cm]	0.3	0.2	0.1
Element count	/	61,000	148,000	615,000
Simulation time for 5 cycles	[h]	15	26	42.5
Inlet volume flow rate	[L/min]	408.6	388.6	371.4
Volume flow rate error	%	13.19	7.65	2.88

0.5%, Eventually, the time step 5.0E-6 was chosen for the simulation of claw pump.

$$Error = \frac{P - 10.86}{10.86} * 100$$

$$Error = \frac{T - 482.35}{482.35} * 100$$

3

Mesh independence study

The cut cell cartesian method utilizes a global mesh size parameter to control the global mesh sizing and properties. The number of the mesh is very sensitive to this parameter. The solution should be independent of the mesh resolution. The mesh independence study is very important to decide the proper global mesh size. Three cases with increasing number of elements were simulated to evaluate the mesh independence. The mesh number is adjusted by the global mesh size.

The maximum number of elements of three cases are 10.3k, 15.8k, and 22.0k elements individually and minimum 3.5k, 5.6k and 8.1k elements individually as shown in Fig. 3.

As shown in Table 3, both pressure and temperature errors are very low of the order of 0.05% in all the three mesh sizes. This can be considered as high numerical accuracy level. However, the setup of the medium mesh size was used for further analysis since temperature error was the least at this mesh size.

First, the volume conservation is compared for three different mesh sizes. The maximum volume error of three cases is around 0.97%. This demonstrates that volume conservation is not sensitive to the mesh size. In addition, the change of volume error with cycles can be ignored because with the increasing of the cycle number, the maximum volume error is around 0.97%. There is a phenomenon that the volume error decreased first then increase while the fine mesh count remained consistent. All the mesh sizes are sufficiently accurate and consistent to describe the chamber volume.

The pressure variation of three cases is shown in Fig. 4 (a), the pressure matched well with the analytic solution for three continuous cycles. Fig. 4 (b) shows the error in cyclic pressure predictions for three continuous cycles. The pressure error increased with the number of cycles because of the accumulated error.

The numerical accuracy level of the cut cell method was thus found to be suitable to use this technique for a practical pump application with complex rotor geometry.

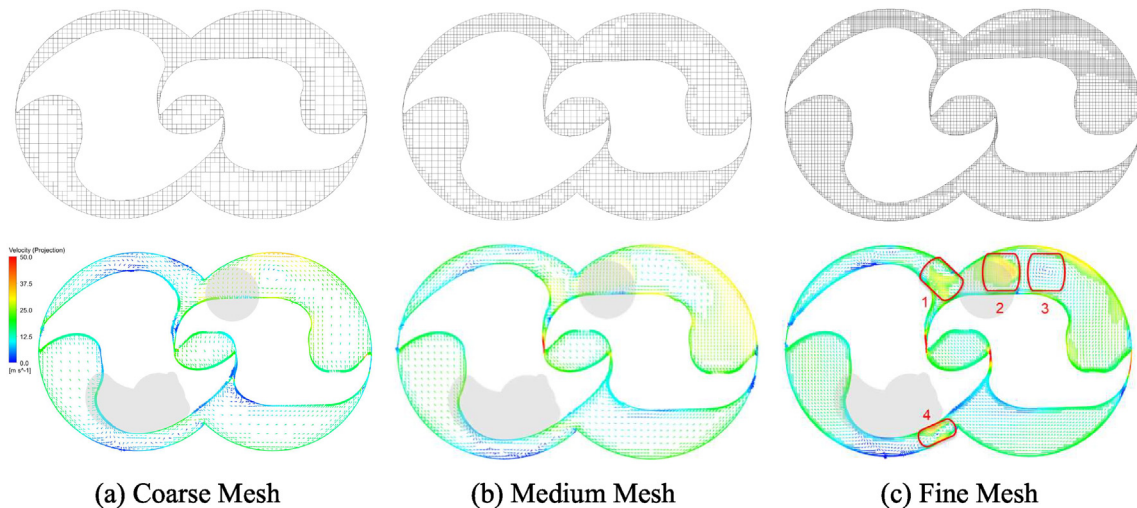


Fig. 6 – The mesh and velocity distribution results of varying mesh sizes.

Table 7 – Cycle comparison.

	Unit	Cycle1	Cycle2	Cycle3	Cycle4	Cycle5
Volume flow rate	L/min	384.2	372.3	370.8	372.2	371.5
Error	%	6.4	3.1	2.7	3.1	2.9

Table 8 – Simulation results comparison.

Variables	Unit	Case1	Case2	Case3	Case4
Discharge pressure	[bar]	1.01	1.11	1.21	1.31
Simulation power	[W]	90.2	102.1	144.3	199.5
Simulation inlet volume flow rate	[L/min]	371.4	320.6	287.2	261.8
Experimental inlet volume flow rate	[L/min]	361.0	321.1	288.6	268.4
Difference between simulation and experiment	[%]	2.88	−0.16	−0.49	−2.46

The simulation of hook and claw pumps

Air and hydrogen supply systems play important roles in the proton electrolyte membrane fuel cell (PEMFC) systems [38]. However, relatively little research has focused on the air and hydrogen supply systems' working parameters such as pressure, temperature and mass flow rate, which will have a significant impact on the performance of PEMFC systems. Computational fluid dynamics combined with Taguchi method, as the optimization tool of the working parameters, have been utilized for the performance prediction of a scroll-type hydrogen pump [3,39] and a claw-type hydrogen pump [8,9]. In this session, a cut cell cartesian mesh has been used for the CFD simulation of the claw-type pump. The velocity and temperature distribution have been much more clearly captured using less mesh compared with body-fitted mesh.

Rotor geometry

The geometry of a typical hook and claw pump is shown in Fig. 5. The drive motor connects with the main rotor through synchronizing gears. Hence there is a clearance between main and gate rotor and no direct contact occurs. The two rotors rotate in opposite directions in the casing to accomplish the suction, transport, internal compression, and the discharge process. The main rotor rotates clockwise, and gate rotor rotates anti-clockwise. The suction and discharge ports are on the same axial side. The internal compression ratio can be varied by adjusting the discharge port position and area.

The claw pump rotor geometry parameters are listed in Table 4. The main rotor and gate rotor have same outer and inner circle diameters. The clearances between rotors and casing in axial direction are 0.08 mm the clearances between rotors and casing in radial direction is 0.07 mm the clearances between main and gate rotor is 0.08 mm.

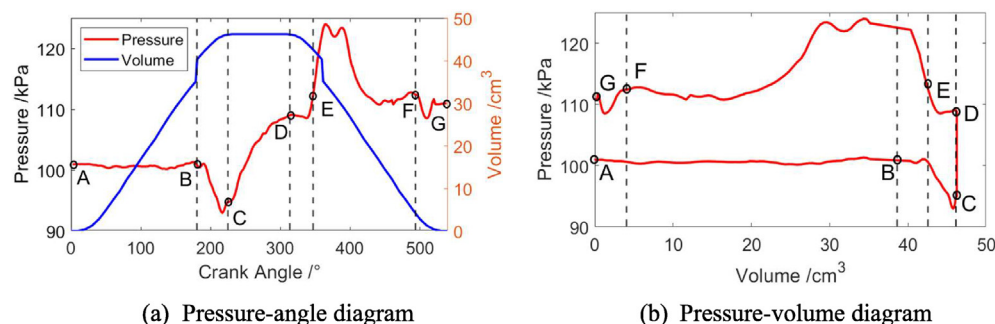
ANSYS forte solver setup

The pump's operating condition specifications are listed in Table 5. This case study did not consider the heat transfer, for example, between the casing wall and environment, the outlet wall and the environment and the rotors and chamber. All boundary walls were thus set as adiabatic. The inlet pressure is set as 1.01 bar, which matches the experimental conditions, while the outlet pressure is varied in the range 1.01–1.31 bar as tested during the experiments.

Mesh independent study

Based on the preliminary study, three global mesh sizes are chosen as listed in Table 6. The suction and discharge pressure are 1.01 bar. The experimental inlet volume flow rate is 361 L/min with discharge pressure of 1.01 bar. The volume flow rate error was calculated based on equation $Error = \frac{V-361}{361} * 100$. Fine mesh size can reach high accuracy and suitable simulation time.

The cartesian cut cell mesh is generated automatically based on the global mesh size and adaptive mesh refining

**Fig. 7 – The Pressure variation with angle and volume.**

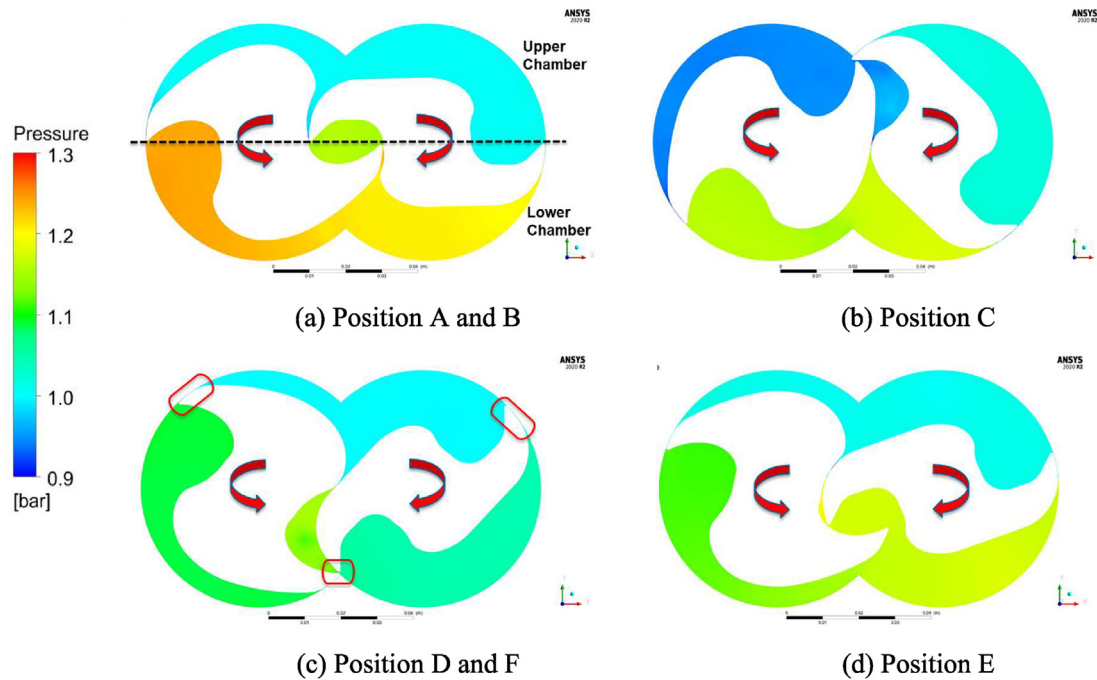


Fig. 8 – The gas pressure contour in the mid plane.

setting. The mesh refinement based on temperature and velocity gradients can be seen in Fig. 6 with three different mesh size. Coarse mesh and medium mesh were not able to capture the details of flow vortices and higher-pressure gradients compared to the Fine Mesh case. As shown in Fig. 6 (c), the pressure gradient was captured in the red square 1 and 2 and the vortices was captured in the red square 3 and 4.

The volume flow rate is also compared for every rotational cycle to check the convergence of the simulation. The inlet volume flow rate and outlet volume flow rate changing with the rotation angle show a repetitive trend after 180° crank angle. Five cycles were calculated for the fine mesh case. To check the convergence accuracy, the time averaged inlet volume flow rate was calculated and compared for individual cycles. The volume flow rate and error compared with the

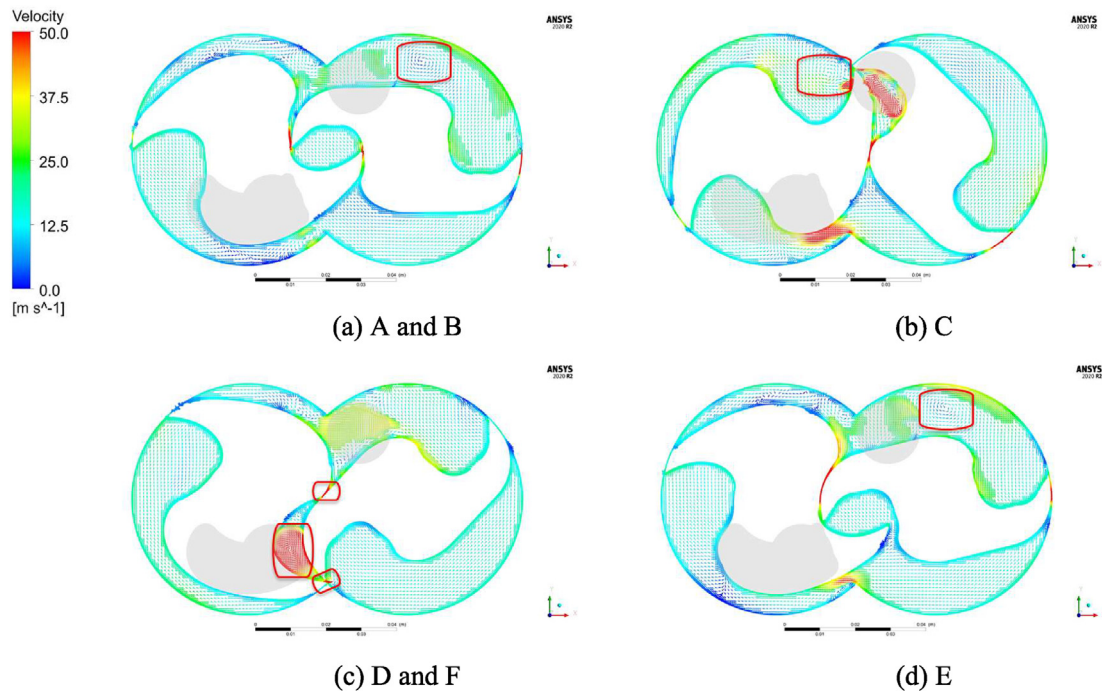


Fig. 9 – The velocity distribution in the middle plan.

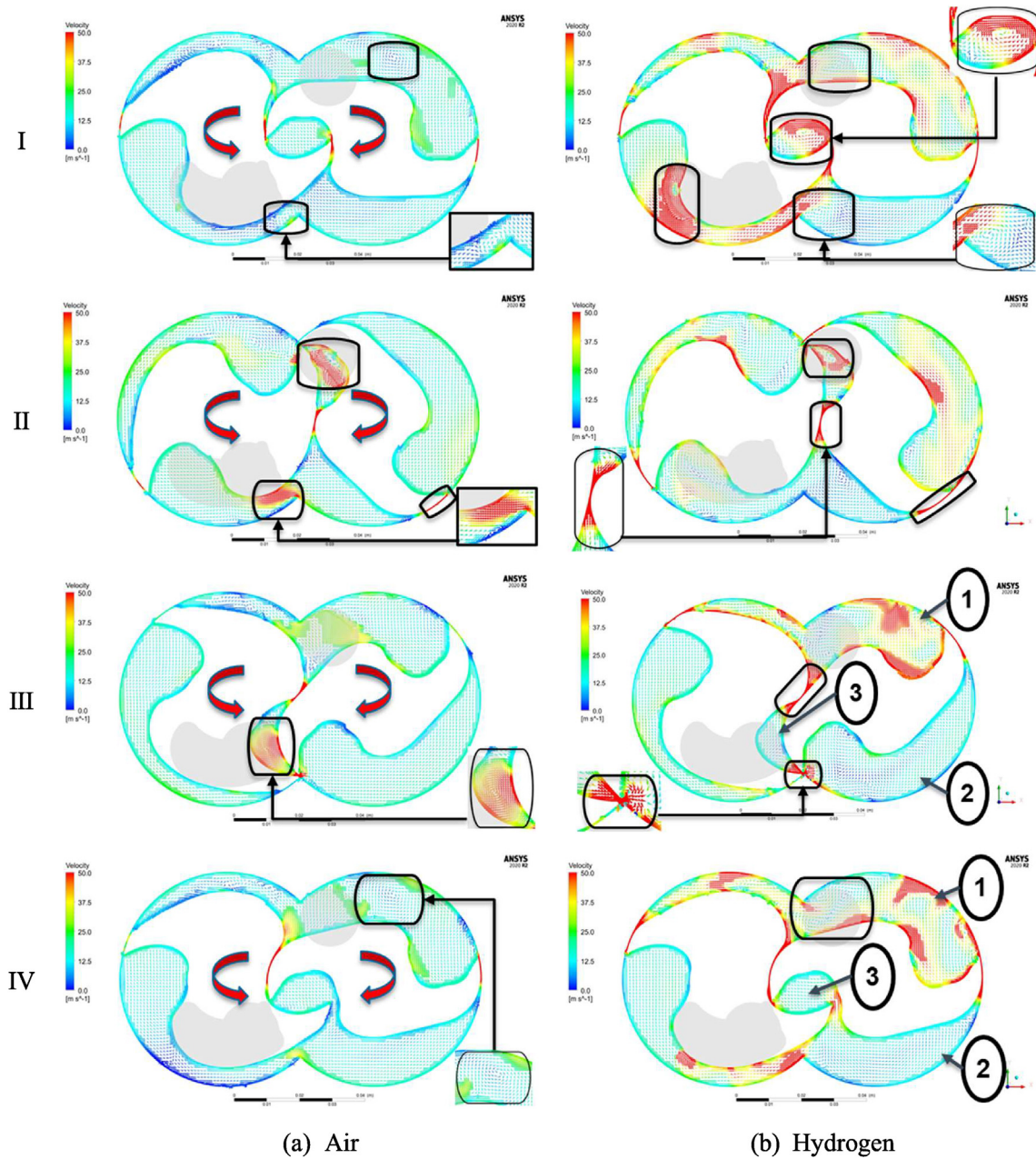


Fig. 10 – The velocity distribution comparison.

experimental results are shown in Table 7. The volume flow rate becomes stable after the cycle 1 and the error is around 3% for the subsequent cycles which is a practically acceptable accuracy level.

Study with varying fluids and operating conditions

To study the pressure and velocity variation inside the claw pump under different working conditions, four cases with different outlet pressure were simulated and compared with the experimental results. The working fluid is air. The other parameters are the same as listed in Table 5. In addition, the case study with hydrogen as the medium was simulated to show the difference with the air.

Case study with air

The power was calculated based on the rotor torque as shown in Eq. (4).

$$P = \frac{2\pi n(T_{main} + T_{gate})}{60} \quad 4$$

The power and volume flow rate were calculated and listed in Table 8. The power consumption is seen to increase with the discharge pressure, while the inlet volume flow rate decreases. The error between simulation and experiment changes from 2.88% to –2.46%. The volume flow rate is over predicted in the simulation for Case1. This is likely an effect of the leakage model. The predicted volume flow rate decreased with the increase of the discharge pressure. This is

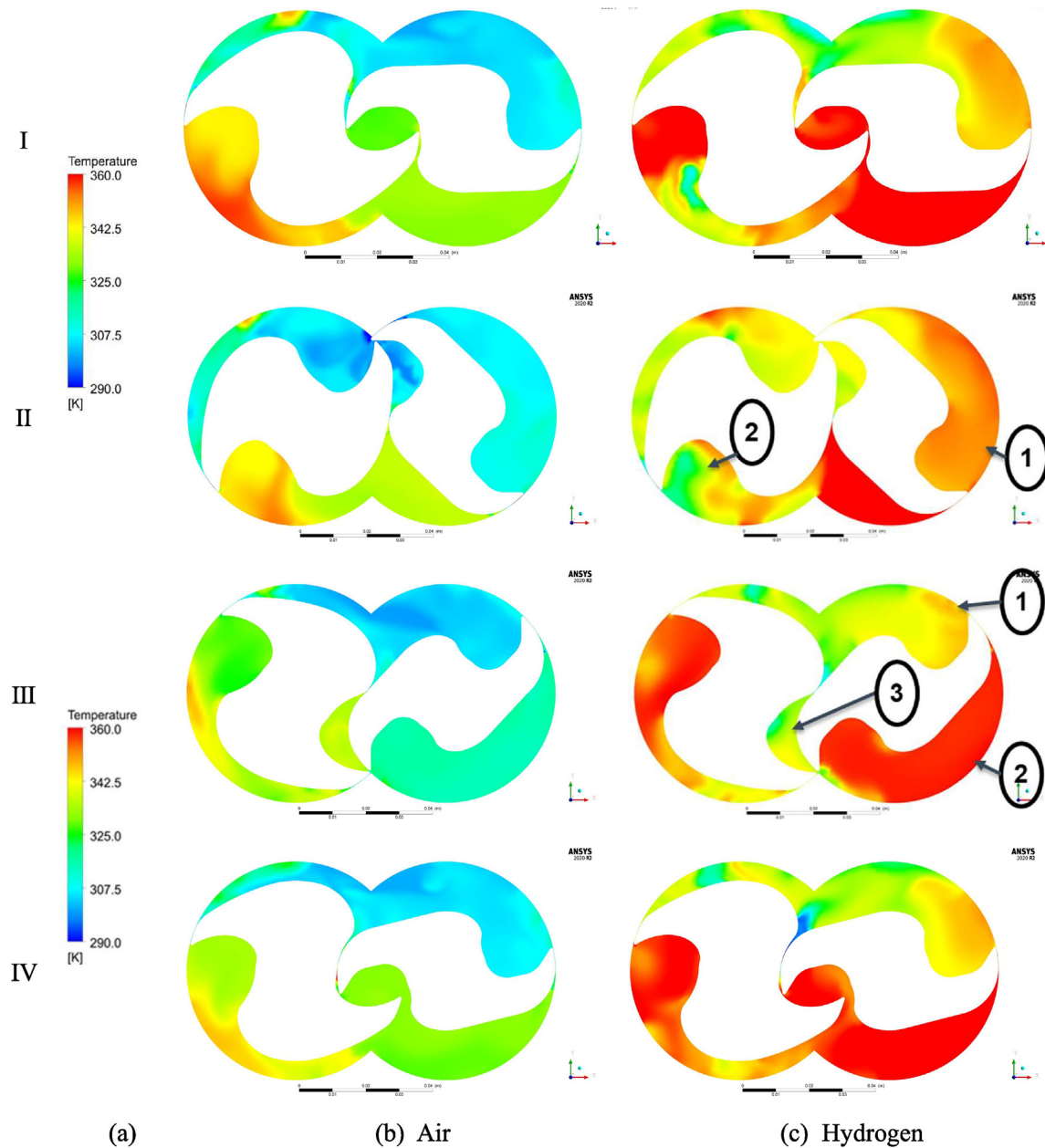


Fig. 11 – Comparison of the Temperature distribution in mid plane.

because the leakage flow is higher in the simulation. A possible explanation for this might be the clearances become smaller when the discharge pressure is higher in the experiment while the clearances keep constant in simulation.

To study the internal flow, 7 probes are set to monitor the pressure inside the chamber. The positions are shown in Fig. 5. P1 is set near the suction port and P7 is set near the discharge port. The interval between remaining probes is 60° . By picking up the valid pressure of each probe and connecting the pressure according to the rotational angle, the pressure-angle diagram can be obtained as shown in Fig. 7 (a). Then, the pressure-volume diagram can be obtained by matching the pressure with the volume. The suction process is AB followed by pressure drop process BC because of the additional

chamber added to the chamber. Then, the chamber volume keeps constant at CD with pressure increasing because of the leakage. The internal compression started at point D and finished until E followed by the discharge process.

The pressure contour in the middle plane is shown in Fig. 8. The starting position is A where the suction starts. The rotors return to the same position after 180° as shown in Fig. 8 (a). In the lower chamber, the pressure of gate rotor chamber is higher than the main rotor chamber even though the two chambers are connected, which means there is pressure variation in the same chamber. Pressure starts to increase, and the main and gate rotor chamber start to separate from position C as shown in Fig. 8 (b). The internal compression starts from position D as shown in Fig. 8 (c). The pressure of

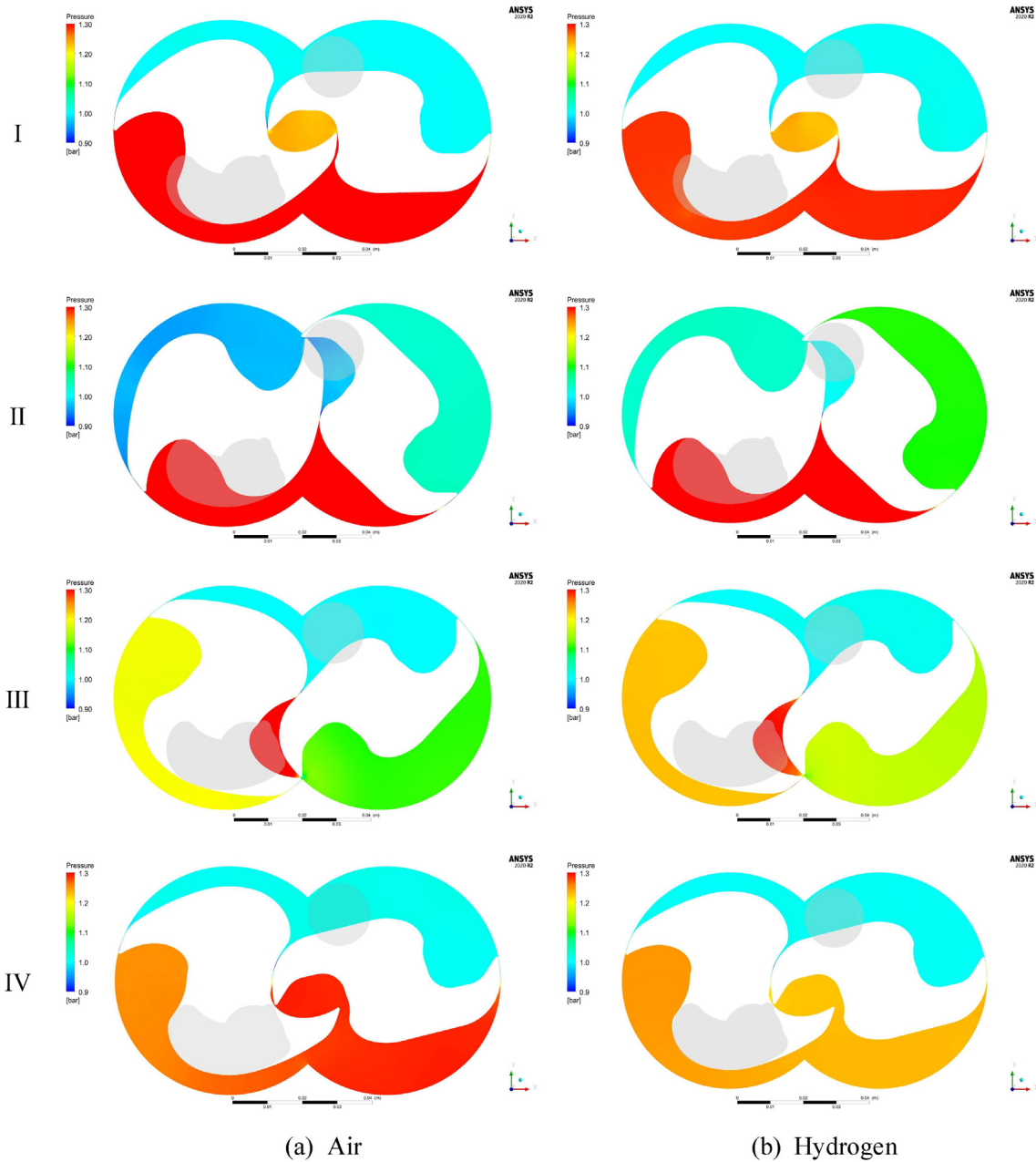


Fig. 12 – Comparison of the Pressure distribution in mid plane.

gate rotor chamber is higher than the main rotor chamber because of the volume difference. The pressure contour at discharge position is shown in Fig. 8 (d).

The velocity vector distribution in the middle plane is shown in Fig. 9. The vortices and leakage flow can be tracked. The vortices are marked using red rectangle. Fig. 9 shows the strong vortices near the discharge port and the leakage flow at cycloid meshing area.

Case study with hydrogen

The velocity, temperature and pressure are compared with air and hydrogen as the working medium. The air and hydrogen properties are listed in Table 1. The density and dynamics viscosity of air is around 14 times and 2 times of hydrogen

separately. The thermal conductivity and specific heat capacity of hydrogen is around 7 times and 14 times of the air individually.

For a discharge pressure of 1.31 bar, the velocity results for the air and hydrogen cases are compared in Fig. 10. The hydrogen case has more high velocity vectors than the air case overall. In stage I of the hydrogen case, high velocity can be observed near the discharge port and interlobe clearance. There is a main vortex generated near the suction port, blow-hole area, discharge port and casing lower tip. The hydrogen case has higher velocity than the air case at the rotor-to-casing clearance and rotor-to-rotor clearance in stage II. High velocity can be observed near the suction port. The fluid direction is from the gate rotor to main rotor. Stage III is the compression

process. In this position, there are three chambers formed at the start of the compression. There is a strong vortex in chamber 3 for the air case. The leakage direction is from chamber 3 to chamber 1 and chamber 2 because of the pressure difference between chambers. Stage IV is the discharge process. Chamber 2 and chamber 3 are connected when the discharge port is open. There may be leakage flow to the blowhole area which will add to the suction chamber.

The temperature calculated for a discharge pressure of 1.31 bar was compared as shown in Fig. 11. The hydrogen case has higher temperatures in the chamber. Stage I is the suction process. The upper chamber has lower temperature than the lower chamber. The temperature inside the chamber is not uniform. The hydrogen case has lower temperature near the discharge port because of the higher local velocity near the discharge port. The suction chamber temperature increased in stage II because of the leakage. The compression stage starts from stage III. The air case has higher temperature in the gate chamber while lower temperature occurs for hydrogen case. The temperature has good mixture after this stage. This can be observed in the stage IV.

The pressure distribution at a discharge pressure of 1.31 bar was compared as shown in Fig. 12. A similar pressure distribution is seen for two cases in stage I. The hydrogen case has higher pressure in the suction chamber compared to the air case in stage II. The main rotor chamber has higher pressure than the gate rotor chamber in both cases. In stage III, the gate rotor chamber pressure is higher than in the main rotor chamber because of the leakage from the discharge port to the gate rotor chamber. In stage IV, pressure variation can be observed in the main and gate chambers when two chambers are connected. With air a higher pressure is found within the main rotor chamber while hydrogen produces a higher pressure within the gate rotor chamber. It is anticipated there is a pressure pulsation within the rotor chamber before the discharge port is open. This could be the cause of difference in instantaneous pressure magnitudes.

The inlet volume flow rate and power for the air and hydrogen cases are compared in Table 9. The hydrogen case has slightly higher inlet volume flow rate and power. It is because a gap flow resistance factor is used in the setup of ANSYS Forte CFD solver in this study. The gap resistance factor is a function of gap size h , the kinematic viscosity ν , and the CFD time step Δt as shown in Eq. (1). Δt is constrained as same value in both air and hydrogen cases. However, kinematic viscosity of hydrogen is around 10 times higher than air. This causes a higher resistance factor and lower $U_{decelerated}$ resulting in an effectively lower leakage in hydrogen case. The experimental data could be used to calibrate the gap resistance factor in the future.

Table 9 – Comparison of volume flow rate and power.

Parameters	Unit	Air	Hydrogen
Inlet volume flow rate	[L/min]	261.8	264.7
Power	[W]	199.5	201.8
Specific Power	[W/L/min]	0.7620	0.7623
Volumetric efficiency	%	47.2	47.7

These results show that the cut cell cartesian method has been successfully tested for the claw-type pump case and provided useful data to enable improvement of the pump and performance optimization.

Conclusions

In this research, the cut cell cartesian mesh generated in ANSYS Forte has been evaluated for numerical accuracy and feasibility for a complex hook and claw pump application. Firstly, an adiabatic compression and expansion process in a simple piston cylinder was studied in detail. The conservation accuracy of the cut cell method was demonstrated. In the second part of the study, the claw pump was simulated under different discharge pressures and the inlet volume flow rate was compared to the experimental results. Additionally, two fluids air and hydrogen were analyzed under 1.31 bar discharge pressure. The flow field data of velocity vectors, gas temperature and pressure contours were compared. The following conclusions can be drawn from these studies:

- The cut cell cartesian mesh satisfied with the volume conservation and the pressure and temperature error is less than 0.05% for the piston cylinder case using medium mesh size.
- The cut cell cartesian mesh has been successfully implemented in the claw pump. Automatic mesh generation (AMG) method enables the simulation setup much simpler and adaptive mesh refinement (AMR) method enables to capture the velocity, temperature and pressure variation more clearly.
- For the claw pump under the same working conditions, the volume flow rate error is consistent after the first cycle and accuracy is around 3%. Under different discharge pressures, the volume flow rate error is within 3% compared with the experimental results.
- The P-theta diagram shows a pressure dip during the suction process. It is suggested that to enlarge the inlet port to reduce the suction loss. The discharge port is suggested to open later after blow hole is disconnected with the discharge chamber.
- The volume flow rate and power of air case is comparable with the hydrogen case. The findings of this study suggest that considering the safety reason, the air could be used for the experiment to measure the volume flow rate and power.
- The cut cell cartesian method is readily applicable and reliable to evaluate the performance of hydrogen claw pump and porting configuration, examine temperature, velocity and pressure distribution.

Declaration of competing interest

The authors declare that they have no known competing financial interests or personal relationships that could have appeared to influence the work reported in this paper.

Acknowledgments

This research was supported by China Scholarship Council and the Centre for Compressor Technology at City, University of London. Authors would appreciate Ningbo Baosi Energy to provide experimental data for CFD validation.

REFERENCES

- [1] Abe JO, Popoola API, Ajenifuja E, Popoola OM. Hydrogen energy, economy and storage: review and recommendation. *Int J Hydrogen Energy* 2019;44:15072–86. <https://doi.org/10.1016/j.ijhydene.2019.04.068>.
- [2] Wilberforce T, El-Hassan Z, Khatib FN, Al Makky A, Baroutaji A, Carton JG, Olabi AG. Developments of electric cars and fuel cell hydrogen electric cars. *Int J Hydrogen Energy* 2017;42:25695–734. <https://doi.org/10.1016/j.ijhydene.2017.07.054>.
- [3] Zhang Q, Feng J, Zhang Q, Peng X. Performance prediction and evaluation of the scroll-type hydrogen pump for FCVs based on CFD–Taguchi method. *Int J Hydrogen Energy* 2019;44:15333–43. <https://doi.org/10.1016/j.ijhydene.2019.04.019>.
- [4] Li J, Jia X, Wu Z, Peng X. The cavity profile of a diaphragm compressor for a hydrogen refueling station. *Int J Hydrogen Energy* 2014;39:3926–35. <https://doi.org/10.1016/j.ijhydene.2013.12.152>.
- [5] Feng J, Xing L, Wang B, Wei H, Xing Z. Effects of working fluids on the performance of a roots pump for hydrogen recirculation in a PEM fuel cell system. *Appl Sci* 2020;10:8069. <https://doi.org/10.3390/app10228069>.
- [6] Xing L, Feng J, Chen W, Xing Z, Peng X. Development and testing of a roots pump for hydrogen recirculation in fuel cell system. *Appl Sci* 2020;10:8091. <https://doi.org/10.3390/app10228091>.
- [7] He Y, Xing L, Zhang Y, Zhang J, Cao F, Xing Z. Development and experimental investigation of an oil-free twin-screw air compressor for fuel cell systems. *Appl Therm Eng* 2018;145:755–62. <https://doi.org/10.1016/j.applthermaleng.2018.09.064>.
- [8] Gu P, Xing L, Wang Y, Feng J, Peng X. A multi-objective parametric study of the claw hydrogen pump for fuel cell vehicles using taguchi method and ANN. *Int J Hydrogen Energy* 2020. <https://doi.org/10.1016/j.ijhydene.2020.11.186>. doi:10.1016/j.ijhydene.2020.11.186.
- [9] Gu P, Xing L, Wang Y, Feng J, Peng X. Transient flow field and performance analysis of a claw pump for FCVs. *Int J Hydrogen Energy* 2020. <https://doi.org/10.1016/j.ijhydene.2020.09.154>. doi:10.1016/j.ijhydene.2020.09.154.
- [10] Hsieh CF. A study of the geometric design and gas port of the claw-type rotor. *Proc IME C J Mech Eng Sci* 2009;223:2063–9. <https://doi.org/10.1243/09544062jmes1452>.
- [11] Hsieh C-F, Hwang Y-W, Fong Z-H. Study on the tooth profile for the screw claw-type pump. *Mech Mach Theor* 2008;43:812–28. <https://doi.org/10.1016/j.mechmachtheory.2007.06.011>.
- [12] Nguyen TL, Wu YR. A novel rotor profile generation method for claw-type vacuum pumps based on sealing line. *Appl Mech Mater* 2019;894:34–40. <https://doi.org/10.4028/www.scientific.net/AMM.894.34>.
- [13] Wang J, Song Y, Jiang X, Cui D, Qu Y. An analytical model of claw rotor profiles and working process model with the mixing process for claw vacuum pumps. *Vacuum* 2015;114:66–77. <https://doi.org/10.1016/j.vacuum.2014.12.029>.
- [14] Stosic N, Hanjalic K. Development and optimization of screw machines with a simulation model-Part2 thermodynamic performance simulation and design optimization. *J Fluid Eng* 1997;119.
- [15] Stosic N, Smith IK, Kovacevic A. *Screw compressor Geometry_Mathematical modeling and performance calculation*. Springer; 2005.
- [16] Peng X, Xing Z, Li L, Shu P. Thermodynamic analysis of the rotary tooth compressor. *Proc IME J Power Energy* 2005;216:321–7. <https://doi.org/10.1243/09576500260251165>.
- [17] Casari N, Fadiga E, Pinelli M, Suman A, Ziviani D. CFD simulations of single- and twin-screw machines with OpenFOAM. *Design* 2020;4:2. <https://doi.org/10.3390/designs4010002>.
- [18] Hsieh C-F, Zhou Q-J. Fluid analysis of cylindrical and screw type Roots vacuum pumps. *Vacuum* 2015;121:274–82. <https://doi.org/10.1016/j.vacuum.2015.04.037>.
- [19] Sun SH, Kovacevic A, Bruecker C, Leto A, Singh G, Ghavami M. Numerical and experimental analysis of transient flow in roots blower. *IOP Conf Ser Mater Sci Eng* 2018;425. <https://doi.org/10.1088/1757-899x/425/1/012024>.
- [20] Kovacevic A, Rane S. Algebraic generation of single domain computational grid for twin screw machines Part II – Validation. *Adv Eng Software* 2017;109:31–43. <https://doi.org/10.1016/j.advengsoft.2017.03.001>.
- [21] Rane S, Kovacevic A. Algebraic generation of single domain computational grid for twin screw machines. Part I. Implementation. *Adv Eng Software* 2017;107:38–50. <https://doi.org/10.1016/j.advengsoft.2017.02.003>.
- [22] Kovacevic A, Rane S, Stosic N. Modelling of multiphase twin screw machines. In: *New technologies. Development and Application*; 2019. p. 18–32. https://doi.org/10.1007/978-3-319-90893-9_2.
- [23] Rane, S.; Kovacevic, A.; Stosic, N.; Stupple, G. Analysis of water evaporation in twin screw compressors using eulerian multiphase approach in CFD. 24th International Compressor Engineering Conference at Purdue, July 9-12, 2018.
- [24] Dong K, Liu G, Yang Q, Zhao Y, Li L, Gao Z. Flow field analysis and performance study of claw hydrogen circulating pump in fuel cell system. *Int J Hydrogen Energy* 2021. <https://doi.org/10.1016/j.ijhydene.2021.08.014>. doi:10.1016/j.ijhydene.2021.08.014.
- [25] Meinke M, Schneiders L, Günther C, Schröder W. A cut-cell method for sharp moving boundaries in Cartesian grids. *Computers & Fluids* 2013;85:135–42. <https://doi.org/10.1016/j.compfluid.2012.11.010>.
- [26] Schneiders L, Hartmann D, Meinke M, Schröder W. An accurate moving boundary formulation in cut-cell methods. *J Comput Phys* 2013;235:786–809. <https://doi.org/10.1016/j.jcp.2012.09.038>.
- [27] Ingram DM, Causon DM, Mingham CG. Developments in Cartesian cut cell methods. *Math Comput Simulat* 2003;61:561–72. [https://doi.org/10.1016/s0378-4754\(02\)00107-6](https://doi.org/10.1016/s0378-4754(02)00107-6).
- [28] Tucker PG, P Z. A Cartesian cut cell method for incompressible viscous flow. *Appl Math Model* 1999;24:591–606.
- [29] Rowinski, D.H.; Li, Y.; Bansal, K. Investigations of automatic meshing in modeling a dry twin screw compressor. 24th International Compressor Engineering Conference at Purdue, July 9-12, 2018.
- [30] Rowinski D, Nikolov A, Brümmer A. Modeling a dry running twin-screw expander using a coupled thermal-fluid solver with automatic mesh generation. *IOP Conf Ser Mater Sci Eng* 2018;425. <https://doi.org/10.1088/1757-899x/425/1/012019>.
- [31] ANSYS. *Forte. Theory Manual* 2021. R1.

- [32] Hartmann D, Meinke M, Schröder W. A strictly conservative Cartesian cut-cell method for compressible viscous flows on adaptive grids. *Comput Methods Appl Mech Eng* 2011;200:1038–52. <https://doi.org/10.1016/j.cma.2010.05.015>.
- [33] Udaykumar HS, Mittal R, Rampunggoon P, Khanna A. A sharp interface cartesian grid method for simulating flows with complex moving boundaries. *J Comput Phys* 2001;174:345–80. <https://doi.org/10.1006/jcph.2001.6916>.
- [34] Tucker PG, Pan Z. A cartesian cut cell method for incompressible viscous flow. *Appl Math Model* 1999;24.
- [35] Rane S, Kovacevic A, Stosic N, Kethidi M. Grid deformation strategies for CFD analysis of screw compressors. *Int J Refrig* 2013;36:1883–93. <https://doi.org/10.1016/j.ijrefrig.2013.04.008>.
- [36] Holmes B. *CFD analysis and ANSYS solutions for positive displacement machines.* City, University of London; 2021.
- [37] ANSYS. *Forte. Tutorials 2021. R1.*
- [38] Zhao Y, Liu Y, Liu G, Yang Q, Li L, Gao Z. Air and hydrogen supply systems and equipment for PEM fuel cells: a review. *Int J Green Energy* 2021;1–18. <https://doi.org/10.1080/15435075.2021.1946812>. doi:10.1080/15435075.2021.1946812.
- [39] Zhang Q, Feng J, Wen J, Peng X. 3D transient CFD modelling of a scroll-type hydrogen pump used in FCVs. *Int J Hydrogen Energy* 2018;43:19231–41. <https://doi.org/10.1016/j.ijhydene.2018.08.158>.